Materials Today Chemistry 50 (2025) 103178

Contents lists available at ScienceDirect

Materials Today Chemistry

journal homepage: www.journals.elsevier.com/materials-today-chemistry/

Functionalization of magnetotactic bacteria with gold Nanoprisms. A Route to novel photothermal agents

Laura Cerezo-Collado [a], Emilio Gómez [a], Yilian Fernández-Afonso [b,1], Ana González [a], Lucía Gutiérrez [b], Jesús M. de la Fuente [b], Ana Abad [c], Alicia G. Gubieda [c], Ma Luisa Fdez-Gubieda [d], Jose M. Dominguez-Vera [a], Víctor Garcés [a,2,*]

[a] Dpto. de Química Inorgánica and Instituto de Biotecnología, Universidad de Granada, 18071, Granada, Spain
[b] Instituto de Nanociencia y Materiales de Aragón, Universidad de Zaragoza-CSIC y CIBER-BBN, 50018 Zaragoza, Spain
[c] Dpto. Inmunología, Microbiología y Parasitología, Universidad Del País Vasco (UPV/EHU), 48940, Leioa, Spain
[d] Dpto. Electricidad y Electrónica, Universidad Del País Vasco (UPV/EHU), 48940, Leioa, Spain

ARTICLE INFO

Keywords:
Magnetotactic bacteria
Gold nanoprisms
EPS
Photothermal therapy
Biohybrid microrobots

ABSTRACT

Magnetotactic bacteria offer promising biomedical applications due to their unique ability to synthesize magnetic nanoparticles and their natural magnetotaxis, which enables their controlled navigation in fluids. They also serve as a platform for integrating synthetic nanomaterials, adding new functionalities and increasing their potential in biomedicine. This study explores the functionalization of *Magnetospirillum gryphiswaldense* (MSR-1) with gold nanoprisms (AuNPR). The attachment of AuNPR to the outer surface of MSR-1 was achieved by two synthetic approaches: i) direct attachment of AuNPR to MSR-1 to produce MSR-AuNPR and ii) pre-coating AuNPR with exopolysaccharides (EPS) from *Lactobacillus plantarum* (Lp) or *Pseudomonas aeruginosa* (Pa), resulting in Lp@AuNPR and Pa@AuNPR, which were then bound to MSR-1, thereby producing MSR-Lp@AuNPR and MSR-Pa@AuNPR. When exposed to near-infrared (NIR) light ($\lambda = 1064$ nm), the functionalized bacteria were able to produce a temperature increase ranging from 8 °C to 10 °C, thereby substantiating their capacity for photothermal therapy. Viability of the functionalized bacteria was also studied. While MSR-1 viability exhibited a greater decrease upon direct AuNPR attachment, EPS-coated AuNPR were able to decrease this toxic effect. This finding suggests that EPS coatings enhance bacterial compatibility and system stability. The study also confirmed that the release of AuNPR from MSR-1 remained minimal under biological pH conditions, indicating a high degree of conservation of the MSR-AuNPR, MSR-Lp@AuNPR, and MSR-Pa@AuNPR systems. Furthermore, the structural integrity of the functionalized bacteria was maintained after prolonged storage at 4 °C. These results underscore the augmented biomedical potential of magnetotactic bacteria functionalized with AuNPR for photothermal therapy, a combination that integrates their mobility given their intrinsic magnetic properties with an innovative NIR-responsive pathway.

1. Introduction

Hyperthermia as a therapeutic approach consists of rising the temperature of a targeted body area (typically ranging from 40 to 43 °C) to produce a therapeutic effect. A considerable amount of research is currently focused on the application of hyperthermia to target cancerous cells while preserving the surrounding healthy tissue [1]. An effective approach involves the use of hyperthermia agents within the tumor to facilitate the conversion of various forms of energy into heat [2]. Among the nanoscale devices with different compositions described for this purpose [3], the most commonly used hyperthermia agents are magnetic nanoparticles and gold nanoparticles, which respectively operate through different mechanisms: magnetic hyperthermia (MHT), induced by alternating magnetic fields (AMF), and photothermal therapy (PTT), triggered by the absorption of near-infrared (NIR) light [4]. The principle of PPT has been demonstrated to be applicable in a variety of

* Corresponding author.
E-mail addresses: vigaro@ugr.es, victor.garces@iit.it (V. Garcés).
[1] Instituto de Ciencia de Materiales de Madrid (ICMM/CSIC), Madrid, Spain.
[2] Italian Institute of Technology, via Morego 30, Genoa 16163, Italy.

https://doi.org/10.1016/j.mtchem.2025.103178
Received 25 July 2025; Received in revised form 9 October 2025; Accepted 31 October 2025
Available online 6 November 2025

therapeutic areas beyond oncology, including bacterial infections, wound healing, ophthalmology, neurological disorders, and cardiovascular diseases [5].

In the field of PTT, anisotropic gold nanoparticles have emerged as a promising solution due to their unique optical properties. Gold nanoprisms (AuNPR) have demonstrated a remarkable ability to absorb light in the NIR range and subsequently convert it into heat. This property makes them especially effective for PTT applications [6], and significant efforts have focused on improving the biocompatibility of AuNPRs—either by attaching organic ligands [7] or by incorporating them into suitable carriers [8] for real-world applications. Notwithstanding the considerable progress that has been made, there are several challenges that have yet to be solved. These include inadequate accumulation and heterogeneous distribution of the particles within solid tumors, inequitable dissipation of heat between distinct tumor regions and the decrease of NIR light reaching PTT agents within the body [9]. In this context, the prospect of biohybrid microrobots, which could be controlled and activated by external stimuli, has been explored as a means of overcoming the limitations of existing PTT agents. In this regard, magnetotactic bacteria have been put forth as biological microrobots called *nanobiots* [10]. This diverse bacterial group comprises a variety of motile aquatic microbes capable of orienting themselves in accordance with the Earth's magnetic field [11]. This phenomenon is attributable to the presence of magnetosomes, which are intracellular magnetic nanoparticles (composed of either Fe_3O_4 or Fe_3S_4) that are biomineralized and arranged into chains along the longitudinal axis of the bacteria [12,13]. The magnetosome chain enables the bacteria to orient themselves in a magnetic field, while motility structures such as flagella facilitate navigation in a directed orientation, a process referred to as magnetotaxis [14]. Magnetotaxis and self-propulsion can be employed to regulate the trajectory of bacterial movement through the utilization of an external magnetic field, while the bacteria actively penetrate deep into tumor tissue [15,16]. Likewise, the presence of the magnetosome chain provides magnetotactic bacteria with intrinsic theragnostic capabilities analogous to those observed in magnetic nanoparticles, such as MHT [17–19]. Moreover, recent findings have revealed that *Magnetospirillum magneticum* (AMB-1) exhibits remarkable photothermal properties in the near-infrared range. The effectiveness of this phenomenon is attributed to the efficient conversion of NIR excitation light into heat by its magnetosome chain [20]. This observation underscores the potential of magnetotactic bacteria to serve themselves as dual hyperthermia agents, capable of generating heat through both alternating magnetic fields and near-infrared light. However, the location of the magnetosomes within the magnetotactic bacteria may ultimately be a limiting factor, as the heat generated is dissipated within the bacteria, with the consequent loss of efficiency to impact the targeted cancer cells. In this regard, it should be noted that hyperthermia agents produce maximum temperature increase at their surface, quickly reducing the effect with the distance from the heating source [21].

In this study, we functionalized the outer membrane of the magnetotactic bacterium *Magnetospirillum gryphiswaldense* (MSR-1) using AuNPR-type gold nanoparticles. Establishing a novel method for producing supplementary heating on the bacteria surface aims to amplifying the therapeutic effect on cancer cells.

The functionalization of magnetotactic bacteria with drugs or nanoparticles has the potential to enhance their properties for biomedical applications. However, only limited progress has been made in this area. Specifically, the uptake of gold nanoparticles (AuNP) by magnetotactic bacteria or their incorporation into the surface of magnetosome has led to the creation of guidable delivery vehicles. These vehicles respond to AMF and NIR light and function as hyperthermia agents [22,23]. However, the use of a microaerophilic strain in the case of bacterial uptake of AuNP has been found to limit the application of AuNP-loaded magnetotactic bacteria in an oxic environment [22]. In a similar manner, isolated AuNP-labeled magnetosomes are incapable of exhibiting the self-propulsion ability characteristic of magnetotactic bacteria. This deficiency results in a reduction of their capacity to penetrate deeper into solid tumors [23]. Furthermore, it has been reported that the magnetosomes produce less heat than the magnetotactic bacteria from which the magnetosomes were isolated [18,24].

AuNPR were externally loaded onto the MSR-1 surface using two different approaches (Scheme 1). The first approach entailed the incorporation of AuNPR into the native outer layer of MSR-1 through a one-pot synthesis. In the layer-by-layer strategy, AuNPR were previously encapsulated in exopolysaccharides (EPS) from different bacterial strains to produce EPS@AuNPR. Subsequently, EPS@AuNPR were integrated onto the external surface of MSR-1. We demonstrate that both approaches result in the functionalization of the external surface of MSR-1 with AuNPR, thereby providing a novel type of externally modified MSR-1. This approach aims at generating additional heat in closer proximity to the tumor cells after NIR irradiation.

We developed a new concept for a bifunctional hyperthermia agent by decorating magnetotactic bacteria (MSR-1) with AuNPRs. The novelty of this system lies in its dual role: MSR-1 provides both the magnetic component, through its intact magnetosome chains, and the platform for assembling gold nanoparticles, which adds the photothermal activity. This represents the first reported functionalization of MSR-1 with AuNPRs, yielding a material capable of heat generation under both magnetic fields and light irradiation. Unlike previous bacteria–nanoparticle conjugates [25], MSR-1 offers advantages as a therapeutic vehicle due to its intrinsic magnetosomes and natural ability to penetrate tumors [10,16]. The resulting hybrid thus stands out as a bimodal agent, adaptable to act through photothermal or magnetic hyperthermia, either separately or in combination, depending on tumor characteristics.

2. Methods

2.1. Materials

All reagents were purchased from Sigma Aldrich.

2.2. Synthesis of gold nanoprisms

Gold nanoprisms (AuNPR) were synthesized following a previously reported protocol [7,25]. 100 ml of $HAuCl_4$ 2 mM and 120 ml of fresh sodium thiosulfate ($Na_2S_2O_3$) 0.5 mM, both prepared in Milli-Q ultrapure water, were mixed and stirred gently at 15 °C. After 9 min ("seed" formation) an extra 50 ml of fresh $Na_2S_2O_3$ 0.5 mM was added. Growth mixture was left overnight at 15 °C under mild stirring conditions. The AuNPR were characterized by UV–vis spectroscopy (using a Thermo Spectronic Unicam UV 300 spectrophotometer), TEM and DLS. Photothermal capacity of AuNPR was also assessed (See Figure SI1 from the Supporting information).

2.3. MSR-1 culture

Magnetospirillum gryphiswaldense MSR-1 (DSMZ 6361) was cultured in flask standard medium (FSM) supplemented with 100 μM of Fe(III)-citrate in three-fourths 15 ml tubes, at 28 °C for 72 h as described elsewhere [26].

2.4. Isolating EPS layer from Lactobacillus plantarum and Pseudomonas aeruginosa

The EPS isolation protocol from *Lactobacillus plantarum* (CECT 220, Lp) was designed based on another probiotic EPS extraction protocol [27]. From an overnight liquid culture of *L. plantarum* grown in de Man, Rogosa and Sharpe medium (MRS, Oxoid) at 37 °C, bacteria were removed by centrifugation at 3000*g* for 10 min. The supernatant was filtered using an EMD Millipore Steritop™ sterile vacuum bottle-top filter (0.22 μm pore size). Ice-cold ethanol (2 vol) was added to the

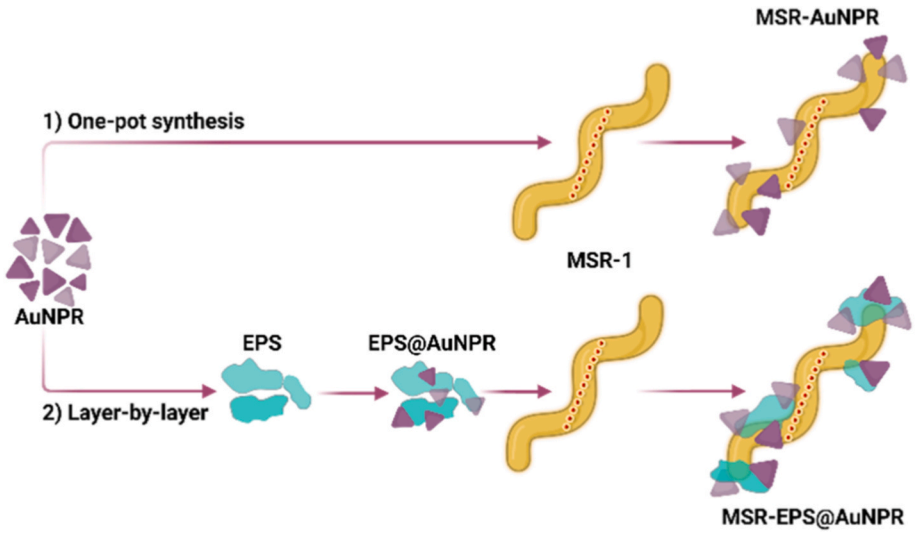

Scheme 1. Gold nanoprisms (AuNPR) were incorporated onto the surface of magnetotactic bacteria *Magnetospirillum gryphiswaldense* (MSR-1), either by direct incorporation (MSR-AuNPR) or previously encapsulated in bacterial EPS in a layer-by-layer approach (MSR-EPS@AuNPR).

cell-free supernatant (1 vol) under continuous stirring, then stored overnight in a refrigerator to promote precipitation. The alcoholic supernatant was centrifuged at 22000 g for 35 min and the precipitated EPS were washed with acetone and centrifuged once again. The solid obtained was dissolved in distilled water (100 ml) and dialyzed against distilled water for 24 h at room temperature using a 12–14 kDa molecular weight cut-off (MWCO). The dialyzed solution was lyophilized.

In the case of EPS from *Pseudomonas aeruginosa* (CECT 108, Pa), a previously reported protocol was carried out with some modifications [28]. 100 ml of a five-days liquid culture of *P. aeruginosa*, grown in tryptic soy broth (TSB No2, Sigma-Aldrich) at 37 °C, were treated with 600 μl of formaldehyde (36.5 % solution). The formaldehyde-bacterial culture mixture was incubated at room temperature with gentle shaking (100 rpm) for 1 h 40 ml of NaOH (1 M) were added and incubated at room temperature, under continuous stirring for 3 h, to extract EPS. Bacterial suspension was then centrifuged (16800 g) for 1 h at 4 °C. The supernatant containing soluble EPS was filtered using an EMD Millipore Steritop™ sterile vacuum bottle-top filter (0.22 μm pore size) and dialyzed against distilled water using a 12–14 kDa MWCO membrane for 24 h at room temperature. Trichloroacetic acid (TCA) was added (6 % w/v) to extracted EPS solutions on ice. After 6.5 h, the solution was centrifuged (16800 g) for 1 h at 4 °C, the supernatant was collected, and 1.5 vol of 96 % ethanol were added, and the mixture was placed at −20 °C overnight to precipitate EPS. The solution was then centrifuged (16800 g) for 1 h at 4 °C and the EPS pellet was resuspended in the minimum amount of Milli-Q water and dialyzed against the same for 24 h at 4 °C using a 12–14 kDa MWCO membrane. The remaining retentate was lyophilized during 24 h.

2.5. Deposition of AuNPR onto EPS layer

0.5 mg ml^{-1} EPS solutions, from *L. plantarum* (Lp) and *P. aeruginosa* (Pa), were separately prepared in water. AuNPR (0.5 vol) were added to the two different EPS solutions (1 vol). All EPS@AuNPR samples were lyophilized and stored as powders. Redissolution of the powders in water gave unchanged UV–vis spectra.

2.6. Grafting AuNPR and EPS@AuNPR to MSR-1

To incorporate AuNPR on MSR-1, an aliquot of an MSR-1 culture (5 ml) was collected and centrifugated at 1500 g for 15 min. 2 ml of AuNPR colloid were added to the bacterial pellet. MSR-AuNPR were collected at 100 g for 30 min, freeze-dried and characterized as mentioned below (see 2.7) [25].

On the other hand, two aliquots of an MSR-1 culture (5 ml) were collected and centrifugated at 1500 g for 15 min. 3 ml of each Lp@AuNPR and Pa@AuNPR colloids were separately added to the two bacterial pellets and incubated at 30 °C for 3 h. The resulting MSR-EPS@AuNPR systems were centrifuged at 100 g for 30 min, freeze-dried and characterized as described in Section 2.7 [25].

The supernatant solutions obtained after the filtration of the mixtures of AuNPR, Lp@AuNPR, and Pa@AuNPR with MSR-1 exhibited no SPR signal corresponding to gold nanoparticles. Consequently, it was ascertained that the absorption percentage to MSR-1 was essentially complete.

2.7. Characterization of AuNPR, MSR-AuNPR and MSR-EPS@AuNPR

To assess the hydrodynamic diameter (dH) and Z potential of AuNPR, dynamic light scattering (DLS) and ζ-potential measurements were performed in water on a Malvern Zetasizer Nano-ZS, using eleven (DLS) and twenty (Z potential) runs per measurement and three replicates at 25 °C.

AuNPR, MSR-AuNPR and MSR-EPS@AuNPR samples were characterized by UV–vis spectroscopy using a Thermo Spectronic Unicam UV 300 spectrophotometer.

Transmission electron microscopy (TEM) analyses were performed with a LIBRA 120 PLUS microscope (Carl Zeiss SMT) operating at 120 keV and a Philips CM-20 HR analytical electron microscope operating at 200 keV. To prepare TEM samples, a drop of the sample was placed on a carbon-coated Cu grid (200 mesh) designed specifically for TEM. The grid was blotted with filter paper. Nanoanalytical information for MSR-AuNPR and MSR-EPS@AuNPR samples were obtained using a FEI Titan Cubed Themis 60-300 microscope operating at 300 kV. The double aberration-corrected scanning transmission electron microscope (STEM) was equipped with a Super X-G2 X-ray energy-dispersive spectrometer (EDX), thus providing a tool to simultaneously combine spectroscopy and image signals. The large area views of the samples were recorded using the scanning high angle annular dark field detector (HAADF).

For the elemental analysis, freeze-dried MSR-AuNPR and MSR-EPS@AuNPR systems were weighed and acid digested for elemental analysis by adding aqua regia ($HCl:HNO_3$, 3: 1 v/v) and heating up to 60 °C for 30 min using a hot block. After that, the samples were allowed to cool down to room temperature and 30 % H_2O_2 (w/v) was added and heated up to 95 °C for 1 h. Inductively coupled plasma optical emission spectroscopy (ICP-OES) was performed to determine the gold

concentrations using a PerkinElmer Optima 2100 DV.

2.8. Photothermal agent characterization

The photothermal conversion was assessed by monitoring the temperature change while the sample (450 μL) was irradiated using a laser (laser quantum, mpc6000/Ventus 1064) of $\lambda = 1064$ nm using a power of 1 W (See Figure SI3 from the Supporting Information). The diluted sample was placed into a quartz cuvette (2 mm optical path) with magnetic stirring and the temperature was recorded with a T-type thermocouple coupled to a Datalogger USB (TC direct). The laser beam (spot size 2.2 mm diameter) corresponds to an irradiated sample volume of 0.008 ml. Given the limited irradiated area, the power density was determined to be 26 W/cm^2. Milli-Q water was used as control. The SAR (kW g_{Au}^{-1}) was calculated using equation (1) [21].

$$\boldsymbol{SAR} = \frac{\boldsymbol{Cp_{H_2O}} \times \boldsymbol{m_{H_2O}}}{\boldsymbol{m_{NPs}}} \times \frac{\boldsymbol{dT}}{\boldsymbol{dt}} \left[\boldsymbol{kWg_{Au}^{-1}}\right] \quad \text{Eq. 1}$$

where C_{pH2O} is the specific heat capacity of water (4.186 J g^{-1} K^{-1}), m_{H2O} is the mass of water (g), m_{NPs} is the mass of Au (g) corresponding to NPs in the irradiated volume (considering the spot size and the cuvette length), and (dT/dt) is the initial slope of the heating curve (first 30 s).

2.9. Release of AuNPR from MSR-AuNPR and MSR-EPS@AuNPR

To assess the conservation percentage of AuNPR from MSR-AuNPR and MSR-EPS@AuNPR, the time-dependent release of gold from samples was analyzed at two physiological pH conditions. At a pH of 7.4, the physiological pH of blood and at a pH of 4.5, simulating the pH inside cell lysosomes [29]. Samples MSR-AuNPR, MSR-Lp@AuNPR and MSR-Pa@AuNPR were prepared as previously described (Section 2.6) and collected by centrifugation at 100*g* for 30 min. Pellets were dispersed in Phosphate Buffered Saline (PBS, 10 mM, 3 ml) at pH 7.4 and pH 4.5, respectively, and incubated at 37 °C during 6h. The amount of released gold (Au_R), after this time, was measured by ICP-OES analysis of 50 μl from all the supernatants after gentle centrifugation (100 g, 30 min). Sample preparation for elemental analysis is detailed above (Section 2.7). To compare with the Au-loading capacity (Au_{LC}) of MSR-1, the same volume of complete samples (not centrifugated, 50 μl) were analyzed by ICP-OES, considering this amount of gold as 100 % of retention. Retention rates (R_R) were obtained according to equation (2).

$$\boldsymbol{R_R} = \boldsymbol{100} - \left[\left(\frac{\boldsymbol{Au_R}}{\boldsymbol{Au_{LC}}}\right)\boldsymbol{x}\ \boldsymbol{100}\right] \quad \text{Eq. 2}$$

To qualitatively evaluate whether released gold results from non-absorbed AuNPR or from the degradation of AuNPR into gold ions, the above-mentioned supernatants from MSR-AuNPR, MSR-Lp@AuNPR and MSR-Pa@AuNPR were characterized by UV–vis spectroscopy using a Thermo Spectronic Unicam UV 300 spectrophotometer. AuNPRs exhibited strong absorption bands in the UV–vis–NIR regions, due to a small particle effect absent in individual gold ions (See Figure SI2 from the Supporting information).

2.10. Electron microscopy study of MSR-AuNPR and MSR-EPS@AuNPR after storage at 4 °C

MSR-AuNPR, MSR-Lp@AuNPR and MSR-Pa@AuNPR were stored for 2 months at 4 °C in PBS (10 mM, 3 ml, pH 7.4). After this period, the sample surfaces were analyzed by Field Emission Scanning Electron Microscopy (FESEM) using a TESCAN AMBER X, instrument located at Centre for Scientific Instrumentation, University of Granada (CIC-UGR). For this purpose, the samples were fixed in 1 mL of 0.1 M cacodylate buffer (pH 7.4) containing 2.5 % glutaraldehyde at 4 °C for 24 h. Subsequently, the samples were washed three times (30 min each at 4 °C) with cacodylate buffer, stained with 1 % (v/v) osmium tetroxide solution for 2 h in the dark, and then thoroughly rinsed with Milli-Q water to remove excess osmium. Dehydration was performed at room temperature using graded ethanol/water mixtures of 50 %, 70 %, 90 %, and 100 % (v/v) for 20 min each, with the 100 % ethanol step repeated three times. Finally, samples were dried at the CO_2 critical point, mounted on quartz wafers, which were placed on conductive carbon tape adhered to metal stubs, and then coated with a thin carbon film. For compositional analysis, the FESEM system is coupled with an Oxford Instruments ULTIM MAX 100 Energy Dispersive X-ray Spectroscopy (EDX) microanalysis system, allowing detailed elemental characterization of the samples.

High-angle annular dark field scanning transmission electron microscopy (HAADF-STEM) images, energy-dispersive X-ray spectroscopy (EDS) spectra, and selected area electron diffraction (SAED) patterns were obtained using a STEM FEI TALOS F200X microscope equipped with four Super-X SDD detectors (Thermo Fisher Scientific, Waltham) at the Scientific Instrumentation Center (CIC-UGR). A carbon-coated copper grid (200 mesh) was gently placed onto a drop of the specific sample. The grids were then rinsed with ultrapure water and allowed air-dry under ambient conditions for 24 h.

2.11. Effect of AuNPR and EPS@AuNPR on the growth of MSR-1

Quantification of AuNPR-loaded bacteria proliferation was performed by using the live/dead bacterial viability kits SYTO9 (green) and propidium iodine (PI) (red) (ThermoFisher) for confocal laser scanning microscopy. 6h after AuNPR and EPS@AuNPR incorporation, MSR-1 were stained with SYTO9 and PI dyes and assessed for viability. Following the manufacturer's instructions, the molar ratio between SYTO9 and PI in the mixture was 1:6. A drop of the AuNPR-decorated bacteria, labeled with both dyes (PI and SYTO9), was deposited onto a polylysine glass and observed in a confocal microscope Leica DMI6000, counting the number of live (green) and dead (red) bacteria in a batch of three experiments with the software Image-Pro Plus 6.0 (Media Cybernetics, Inc., Rockville, MD, USA). The average live/dead ratio was used to quantify the bacterial viability.

Moreover, to evaluate the bacterial growth after AuNPR incorporation, the absorbance at 600 nm (OD600 nm) was measured with a spectrophotometer (Infinite® 200 PRO NanoQuant) every 24 h, and the growth curves were plotted to compare the cytotoxic effects of AuNPR and EPS@AuNPR on the growth of MSR-1. All experiments were repeated three times.

2.12. Antibacterial activity of gold ions in MSR-1

Decreasing concentrations (starting from 2 mM and ending in 0.007 mM) of $HAuCl_3$ were incorporated into 200 μl of FSM in a 96 well-plate. Each well was inoculated with 100 μl of a standardized cell suspension containing 1×10^6 viable bacteria/ml. The inoculated plate was incubated at 28 °C for 72 h, and bacterial growth was measured by means of absorbance at 600 nm.

3. Results and discussion

3.1. MSR-AuNPR and MSR-EPS@AuNPR synthesis

For the one-pot synthesis (Scheme 1), AuNPR were subjected to direct incubation with MSR-1. TEM images of the resulting MSR-AuNPR sample (Fig. 1) demonstrated that AuNPR, both individually and in aggregate form, were distributed over a substantial portion of the MSR-1 surface. The presence of aligned magnetosomes within MSR-1, which were labeled in green in the HAADF-STEM image (Fig. 1B), was also observed. The supernatant solution obtained after centrifugation of MSR-AuNPR did not exhibit SPR signal corresponding to any gold nanoparticle. Moreover, ICP-OES measurements confirmed a negligible presence of gold in the supernatant. Therefore, it was determined that

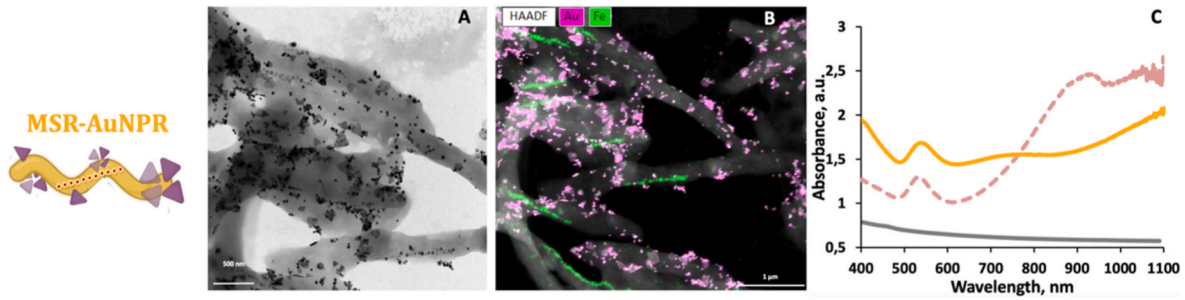

Fig. 1. (A) TEM image of the MSR-AuNPR. (B) HAADF-STEM merged with EDX compositional analysis of the MSR-AuNPR (Au, pink; Fe, green). (C) UV–vis spectra of AuNPR (dashed line) and MSR-AuNPR (orange solid line), MSR-1 was used as control (grey solid line).

the absorption percentage of AuNPR on MSR-1 bacteria was virtually complete. To the best of our knowledge, the only previous example of functionalization of magnetotactic bacteria using gold nanoparticles was based on DNA-AuNP that were internalized by endocytosis in MSR-1. In that case the viability of MSR-1 was compromised under aerobic conditions [22].

UV–Vis spectroscopic analysis of the MSR-AuNPR (Fig. 1C) revealed a shift of the absorption maxima towards lower energies in the near-infrared region (1100 nm) compared to that of the UV–Vis spectrum of isolated AuNPR (935 nm). This shift was attributed to the local aggregation of gold nanoparticles on the bacterial surface. Consequently, MSR-AuNPR exhibited absorption in the NIR region, making it suitable for biomedical applications, as NIR light has the capacity to penetrate deep into soft tissues and reach the nanoparticles within the body [30,31].

In the second approach to functionalize MSR-1, the layer-by-layer approach, AuNPR were precoated with EPS (Scheme 1). This method is particularly interesting due to its potential to create layered systems and provide a more biocompatible coating for the nanoparticles [25]. EPS are a pool of molecules, mainly exopolysaccharides, that surround the outer surface of certain bacteria and are the precursor in the formation of biofilms. The biofilm enables bacterial communities to thrive, thereby enhancing their survival prospects by establishing an optimal environment for communication and defence [32]. In this study, two distinct bacterial strains were selected for their role as EPS producers given their different composition, and properties. Specifically, EPS from *Lactobacillus plantarum*, a Gram-positive bacterium designated as GRAS (generally recognized as safe) probiotic due to its capacity to ferment lactic acid and to exert health benefits after consumption was used [33]. It is worth noting that the ability of EPS from the *Lactobacillus* genus to adhere to gold nanoparticles was previously reported [25]. On the other hand, *Pseudomonas aeruginosa*, a pathogenic bacterium, was selected because it is a gram-negative bacterium, as MSR-I is, and it is widely studied as a model organism for biofilm formation due to its high substrate adhesion capacity [34]. The production of EPS by *P. aeruginosa* is well documented, and its applications in biomedicine have been approved for commercial use [35]. Interestingly, EPS from *P. aeruginosa* are heterogeneous biopolymers (including polysaccharides, proteins, nucleic acids, lipids, and humic substances) that function as key structural components in biofilms, while EPS from *L. plantarum* are mainly polysaccharides with reported bioactive (antioxidant, anti-adhesion, anti-tumor) and technological (gelling, stabilizing) properties [36,37].

AuNPR were first incubated with EPS from *L. plantarum* or *P. aeruginosa*, and the resulting Pa@AuNPR and Lp@AuNPR were then added to MSR-1 to obtain the MSR-Lp@AuNPR and MSR-Pa@AuNPR samples. This second strategy sought to exploit the specific EPS–EPS recognition that allows the layer-by-layer formation of structures on the bacterial outer wall [25]. The HAADF-STEM and EDX studies confirmed that Pa@AuNPR and Lp@AuNPR were adhered to MSR-1 (Fig. 2). Magnetotactic bacteria were easily distinguished by the magnetosome

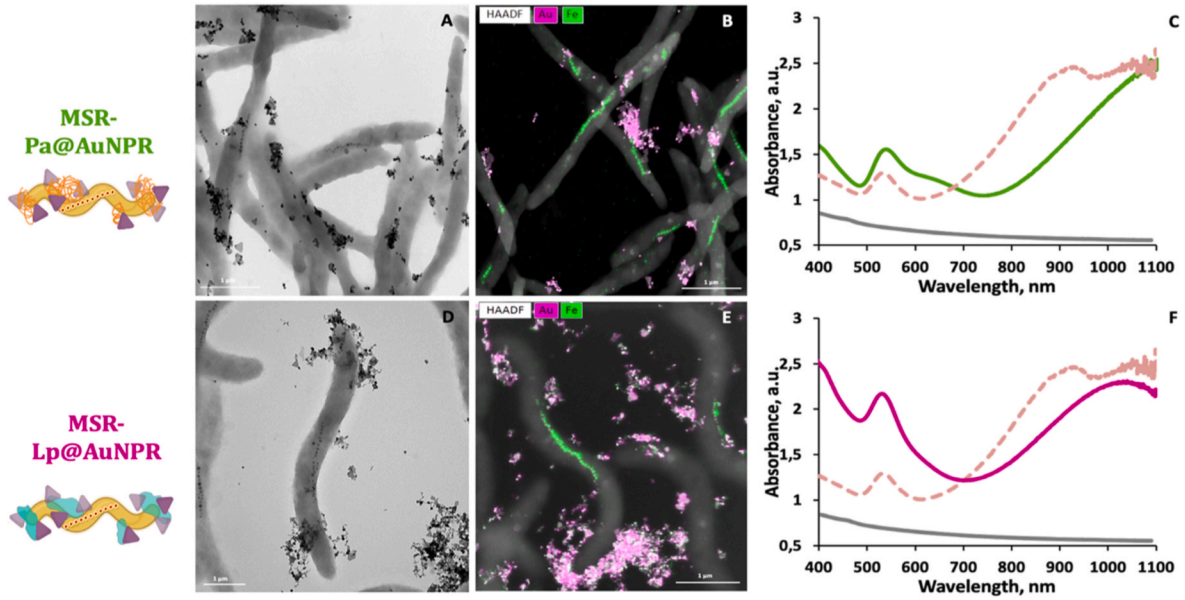

Fig. 2. (A and D) TEM images of MSR-Pa@AuNPR and MSR-Lp@AuNPR respectively. (B and E) HAADF-STEM merged with EDX compositional analysis of MSR-Pa@AuNPR and MSR-Lp@AuNPR respectively (Au, pink; Fe, green). (C and F) UV–vis spectra of MSR-Pa@AuNPR (C, green solid line), MSR-Lp@AuNPR (F, pink solid line) and AuNPR (C and F, dashed line), MSR-1 was used as control (grey solid line).

chains (in green in Fig. 2B and E). In such cases, the EPS@AuNPR layer only partially covered the surface of the MSR-1, following a very similar pattern in both MSR-1@La@AuNPR and MSR-Pa@AuNPR samples. Both samples showed absorption bands in the UV–vis spectra at around 1100 nm and 1050 nm respectively (Fig. 2). The aggregation effect of EPS encapsulation on AuNPR was previously observed [25,27]. The gold content in the supernatant solutions obtained after centrifugation of MSR-1@La@AuNPR and MSR-Pa@AuNPR was found to be negligible, indicating that the absorption of both EPS@AuNPR to MSR-1 was as efficient as for AuNPR.

3.2. MSR-AuNPR and MSR-EPS@AuNPR heating efficiency

Conventional agents for PTT have traditionally been based on gold nanoparticles; however, the use of magnetic nanoparticles as heat sources under NIR light exposure has been explored only in recent years [21,38]. In fact, magnetotactic bacteria *M. magneticum* (AMB-1) were recently tested for photothermal treatments, finding that a higher temperature increase was achieved when irradiating AMB-1 with a NIR light. Thus, in our systems, two different components had the potential to generate heating by NIR irradiation: the native magnetosomes of MSR-1 and the synthetic AuNPRs located on the outer surface. The objective of this study was to assess the heating induced by the AuNPR component. To this end, experiments were conducted at low concentrations of MSR-1 bacteria, approximately $2x10^8$ bacteria/ml and 5 μg/mL of iron. This concentration was notably low, and it was equivalent to a minimal quantity of magnetosomes.

The heating produced by the AuNPR-labeled MSR-1 samples when exposed to a NIR light (λ = 1064 nm) was measured during 5 min. The samples were prepared with the same Au concentration of 0.05 mg_{Au}/mL. The heating curves demonstrated temperature increments of 7.9, 9.8, and 9.3 °C for MSR-AuNPR, MSR-Lp@AuNPR, and MSR-Pa@AuNPR, respectively (see Fig. 3). This increase in temperature allowed reaching values near the 42–45 °C range, which, according to the literature on photothermal therapy and hyperthermia, is considered as the effective thermal window for inducing tumor cell stress while minimizing damage to healthy tissue [39]. Indeed, some relevant related examples found in the literature had shown that gold–iron oxide nanohybrids are able to generate local temperature increases exceeding 42 °C in a 3D glioblastoma model upon near-infrared irradiation, demonstrating that such localized heating was sufficient to induce cell death in tumor-mimicking tissues [40]. Additionally, the complete tumor remission in an animal model was also reported when the tumor temperature (achieved through photothermal treatment) exceeded 43 °C for a sustained period of time [41].

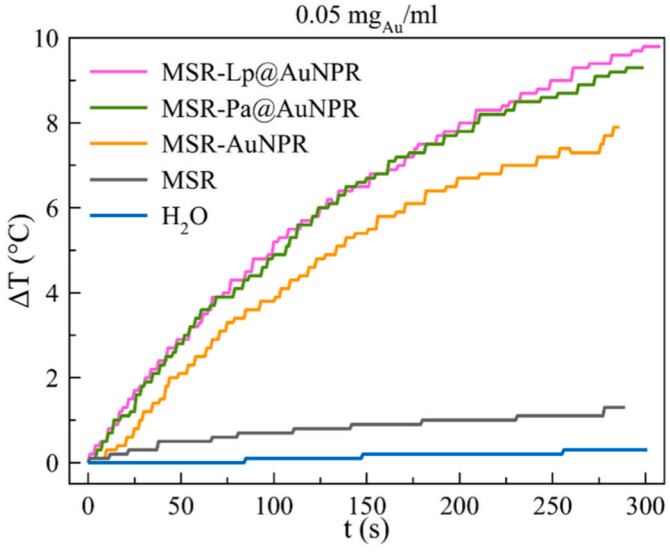

Fig. 3. Heating curves obtained after laser irradiation of MSR-AuNPR, MSR-Pa@AuNPR and MSR-Lp@AuNPR at 0.05 mg_{Au} ml^{-1}, plus water as a control sample. Heating curve of MSR-1 was used as reference (grey solid line).

Notably, at these low bacterial concentrations, the native MSR-1 sample (i.e., magnetotactic bacteria with no AuNPR) exhibited a negligible temperature increase when irradiated under identical experimental conditions. The observed increase in temperature (Fig. 3, grey solid line) was approximately one order of magnitude less than that of the samples containing AuNPR. Therefore, it was concluded that the photoactivated heat generation of MSR-AuNPR, MSR-Lp@AuNPR, and MSR-Pa@AuNPR was mainly due to the presence of adsorbed AuNPR to MSR-1 and not to the MSR-1 magnetosomes.

A recent study by Huang et al. [20] showed that a different strain of magnetotactic bacteria (*M. magneticum*, AMB-1) was used for photothermal treatments, and a higher temperature increase was achieved when irradiating the bacteria with a NIR light. However, several factors may play an important role in achieving such a high temperature increase. The primary factor influencing the observed results and precluding a direct comparison between the two studies is the concentration of bacteria utilized in both investigations. In the present study, approximately $2{\cdot}10^8$ MSR-1 bacteria/mL were used, containing approximately 5 μg/mL of iron. In contrast, the study by Huang et al. [20] used iron concentrations ranging from 100 to 400 μg/mL, which is significantly higher than the concentration used in our experiments. Another crucial element is the experimental design and measurement methodology. In the aforementioned study, the entire sample was irradiated, covering an area of approximately 0.24 cm^2 (equivalent to the dimensions of a 96-well plate). In contrast, our measurement system employed a targeted irradiation of a limited area, representing a fraction of the total sample volume (~1.7 %), while the recorded temperature reflected the overall system average.

The quantities of gold per sample were determined to be 1 %, 1.1 %, and 1.3 % by weight of Au for MSR-AuNPR, MSR-Pa@AuNPR, and MSR-Lp@AuNPR, respectively. The SAR values were derived from the concentration-normalized slopes of the temperature curves (see Experimental Section). Under these measurement conditions, SAR values of 275, 304, and 266 kW/g_{Au} were observed for MSR-AuNPR, MSR-Lp@AuNPR, and MSR-Pa@AuNPR, respectively (see Table 1). The highest SAR value of MSR-Pa@AuNPR was associated with a shift in the absorption maximum in the UV–vis spectrum towards longer wavelengths (Fig. 2C), along with a reduced amount of gold relative to the other samples (Table 1).

Gold nanoprism (AuNPR) deposition was observed on the outer surface of MSR-1, while the internal magnetosome chains remained intact (Fig. 1A and B). This indicates that the structural basis for magnetic hyperthermia (MHT) was preserved. In these hybrid systems (MSR-AuNPR, MSR-Lp@AuNPR, and MSR-Pa@AuNPR), the combination of magnetosomes and gold nanoparticles suggests potential for dual photothermal therapy (PTT) and MHT applications. PTT would arise from both magnetosomes and AuNPR, while MHT would rely on magnetosomes as previously reported [10,18].

3.3. pH effect on AuNPR release from MSR-AuNPR and MSR-EPS@AuNPR

The influence of pH on AuNPR release was investigated to evaluate

Table 1
Summary table showing the mean values of gold concentration in each sample and their corresponding SAR values.

Sample	% Au w/w	SAR (kW/g_{Au})
MSR-Lp@AuNPR	1.3	266
MSR-Pa@AuNPR	1.1	304
MSR-AuNPR	1	275

the stability of MSR-AuNPR, MSR-Lp@AuNPR, and MSR-Pa@AuNPR after a 6-h incubation at 37 °C. Given that variations in physiological pH can influence nanoparticle behavior [42], AuNPR release was assessed under two conditions: pH 7.4, mimicking the bloodstream, and pH 4.5, representative of the mildly acidic tumor microenvironment and/or the lysosomal compartment within cells.

Fig. 4 presents the retention percentages of AuNPR for the three formulations after incubation at both pH values. The released gold content in the supernatants was quantified using ICP-OES, and retention rates were calculated according to Equation (2) (see Section 2.9), by comparing the amount of released gold to the total gold content in the samples. At pH 7.4, retention rates were 90.5 %, 80 %, and 78.5 % for MSR-Pa@AuNPR, MSR-Lp@AuNPR, and MSR-AuNPR, respectively. As anticipated, slightly lower retention was observed at pH 4.5 for all samples, likely due to the more destabilizing acidic conditions. Notably, at physiological pH, the EPS-coated system of *P. aeruginosa* exhibited significantly enhanced AuNPR retention rates compared to the uncoated MSR-AuNPR, suggesting that its EPS coating improves the stability of AuNPR-functionalized MSR-1 under these conditions. In contrast, no significant differences were observed between MSR-Lp@AuNPR and MSR-AuNPR at pH 7.4, whereas the protective effect of L. *plantarum* EPS became apparent under acidic conditions.

These results suggest that EPS coatings derived from *P. aeruginosa* and *L. plantarum* improved the stability of AuNPR-functionalized MSR-1.

To verify that the released gold detected in the supernatants originated from non-absorbed AuNPR rather than from the degradation of AuNPR into ionic gold species, the supernatants of all samples collected at pH 7.4 were analyzed using UV–vis–NIR spectroscopy. The resulting spectra for all samples exhibited characteristic plasmon resonance absorbance bands associated with intact AuNPR, thereby confirming that the released gold corresponded to particulate AuNPRs and not to dissolved gold ions (see Figure SI2). As expected, samples exhibiting higher levels of AuNPR release—specifically MSR@AuNPR—displayed increased absorbance signals in the spectra, consistent with their lower nanoparticle retention ratios.

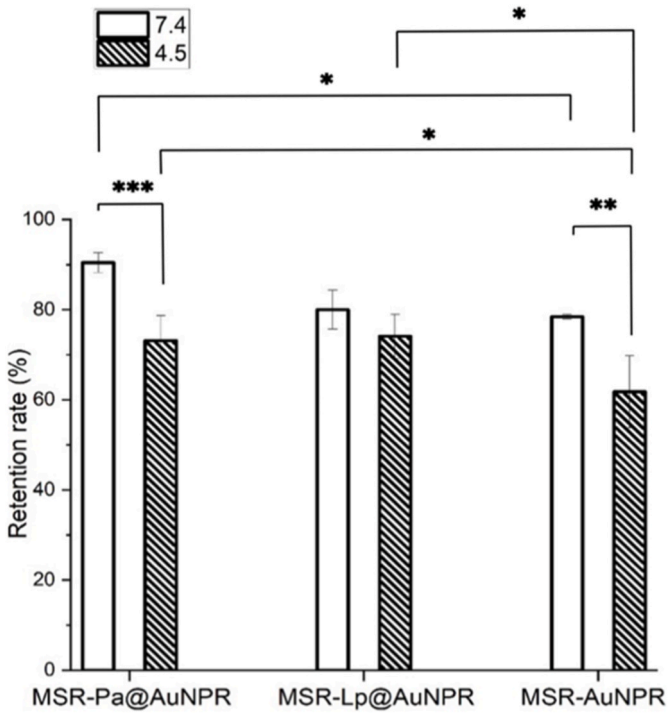

Fig. 4. AuNPR retention rates from MSR-Pa@AuNPR, MSR-Lp@AuNPR, and MSR-AuNPR in Potassium Phosphate Buffer pH 7.4 (empty bars) and in Potassium Phosphate Buffer pH 4.5 (striped bars) after 6h at 37 °C. Statistical significance is indicated by asterisks (**p < 0.05; **p < 0.01; ***p < 0.001*).

3.4. Effect of long-time storage on MSR-AuNPR and MSR-EPS@AuNPR integrity

The structural integrity of the samples was assessed by Field Emission Scanning Electron Microscopy (FESEM) after two months of storage at 4 °C in phosphate-buffered saline (PBS, pH 7.4). As shown in Fig. 5, FESEM images confirmed the continued interaction between AuNPR and the outer surface of MSR-1 in all systems—MSR-AuNPR, MSR-Lp@AuNPR, and MSR-Pa@AuNPR (Fig. 5A–E, and I, respectively). Elemental analysis via energy-dispersive X-ray spectroscopy (EDX) further verified the presence of gold on the surface of MSR-1 across all samples (Fig. 5B–F and J).

The spatial distribution of AuNPR closely resembled that observed in freshly prepared samples (Figs. 1 and 2). In MSR-AuNPR (Fig. 5C and D), AuNPR appeared more diffusely distributed over the bacterial surface. In contrast, MSR-Lp@AuNPR and MSR-Pa@AuNPR (Fig. 5G and H and 5K–L, respectively) exhibited randomly dispersed aggregates of EPS-coated AuNPR. Collectively, these observations indicated that all systems retained their structural integrity and that the interactions between AuNPRs and the MSR-1 outer membrane were maintained after two months of storage at 4 °C in PBS pH 7.4.

Based on both the heating efficiency and the viability of MSR-1 (see Section 3.5), the MSR-Pa@AuNPR sample stored for two months at 4 °C was selected for further characterization by transmission electron microscopy (TEM). High-angle annular dark-field scanning transmission electron microscopy coupled with energy-dispersive X-ray spectroscopy (HAADF-STEM-EDX) analysis (Fig. 6) confirmed the presence of Pa@AuNPR adhered to the surface of MSR-1. As observed in the SEM images (Fig. 5), the Pa@AuNPR only partially covered the bacterial surface.

The HAADF-STEM and EDX results (Fig. 6B and C) further verified this partial surface coverage. Magnetotactic bacteria were easily identified by their characteristic magnetosome chains, highlighted in green in Fig. 6C. Notably, the spatial distribution of the EPS@AuNPR resembled that observed in freshly prepared samples (see Fig. 2B), indicating consistent structural organization despite storage.

3.5. Viability of MSR-AuNPR- and MSR-EPS@AuNPR

The bacterial viability of the three samples (MSR-AuNPR, MSR-Lp@AuNPR, and MSR-Pa@AuNPR) was evaluated using a standard live/dead assay for confocal laser scanning microscopy (CLSM) with the dyes SYTO9 and propidium iodide (PI). Both dyes can bind to bacterial nucleic acids; however, they differ in their ability to penetrate bacterial cells. Propidium iodide (PI) (red) can only penetrate non-viable bacteria with damaged membranes, whereas SYTO9 (green) stains all bacteria. Consequently, the CLSM reveals red fluorescence dots for dead bacteria and green fluorescence dots for live bacteria. Bacteria that appear as both green and red dots in the merged image (red + green channels) are considered dead. The CLSM images obtained for MSR-AuNPR, MSR-Lp@AuNPR, and MSR-Pa@AuNPR are shown in Fig. 7B–D, compared with a control MSR-1 culture without AuNPR (Fig. 7A). The bacterial viability of each sample was quantified by the ratio of the number of green and total spots in the merged channels. Values of 8 ± 6 %, 17 ± 6 %, and 30 ± 8 % were obtained for MSR-AuNPR, MSR-Lp@AuNPR and MSR-Pa@AuNPR, respectively (Fig. 7E). The viability of the control culture of MSR-1 was found to be 99 % ± 1 %.

The survival of MSR-AuNPR was found to be significantly lower than that of MSR-Pa@AuNPR, with a 22 % reduction in the percentage of living cells. This finding suggests that the toxicity of AuNPR to MSR-1 was reduced when encapsulated in EPS. Au^{3+} is widely known to be a cytotoxic agent and therefore it could be speculated that this could be the species causing the low viability levels found. To evaluate this, MSR-1 were exposed to Au^{3+} concentrations ranging from 0.007 to 2 mM.

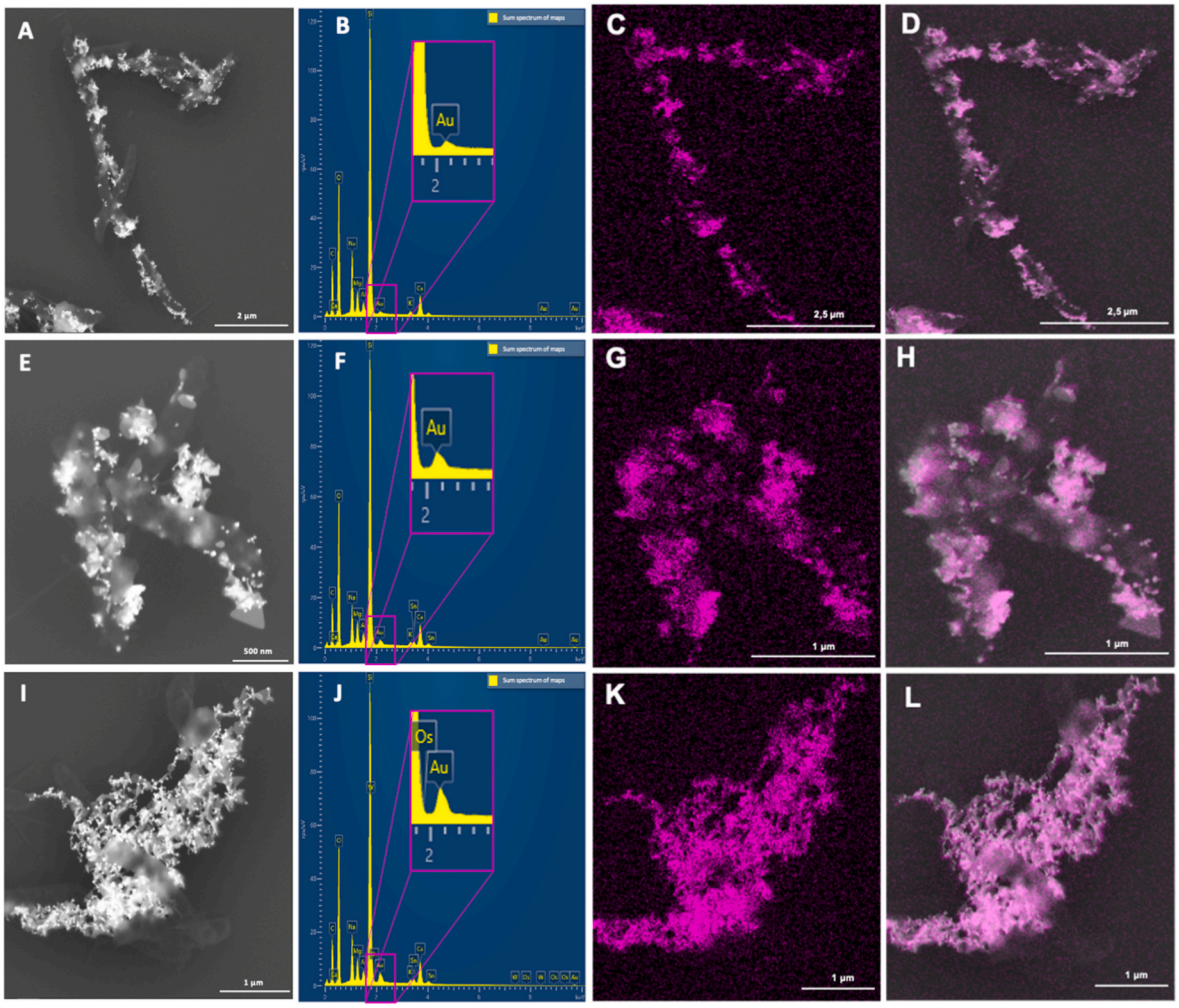

Fig. 5. FESEM micrographs of MSR-AuNPR, MSR-Lp@AuNPR, and MSR-Pa@AuNPR (A, E and I respectively), EDX spectra (B, F and J respectively) and elemental mapping (C, G and K respectively). Gold-related peaks in the spectra are shown as inset zooms. FESEM images combined with EDX compositional analysis (gold in pink) of MSR-AuNPR, MSR-Lp@AuNPR, and MSR-Pa@AuNPR (D, H and L respectively).

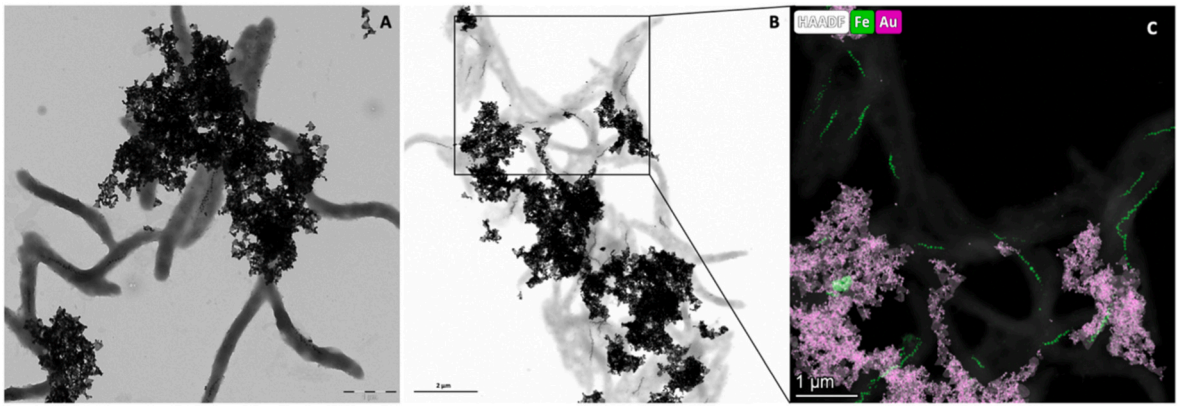

Fig. 6. (A and B) TEM images of MSR-Pa@AuNPR. (C, inset from B) HAADF-STEM merged with EDX compositional analysis of MSR-Pa@AuNPR (Au, pink; Fe, green).

Even at the lowest Au^{3+} concentration, no growth of MSR-1 was detected. The fact that Au^{3+} is a cytotoxic species for MSR-1, and that the presence of EPS mitigates its toxicity is consistent with previous observations related to the reducing capacity of certain EPS in the presence of Au^{3+} ions, resulting in the formation of gold nanoparticles [27]. Therefore, the enhanced reducing potential of EPS could be postulated as a contributing factor to the reduced toxicity of EPS@AuNPs to MSR-1 and suggests that the use of EPS coating is a useful way to introduce potential cytotoxic agents into bacteria with a lower impact on their viability. However, no significant differences were observed between the viability of MSR-AuNPR and MSR-Lp@AuNPR. These results are consistent with the retention rate (Fig. 4), indicating

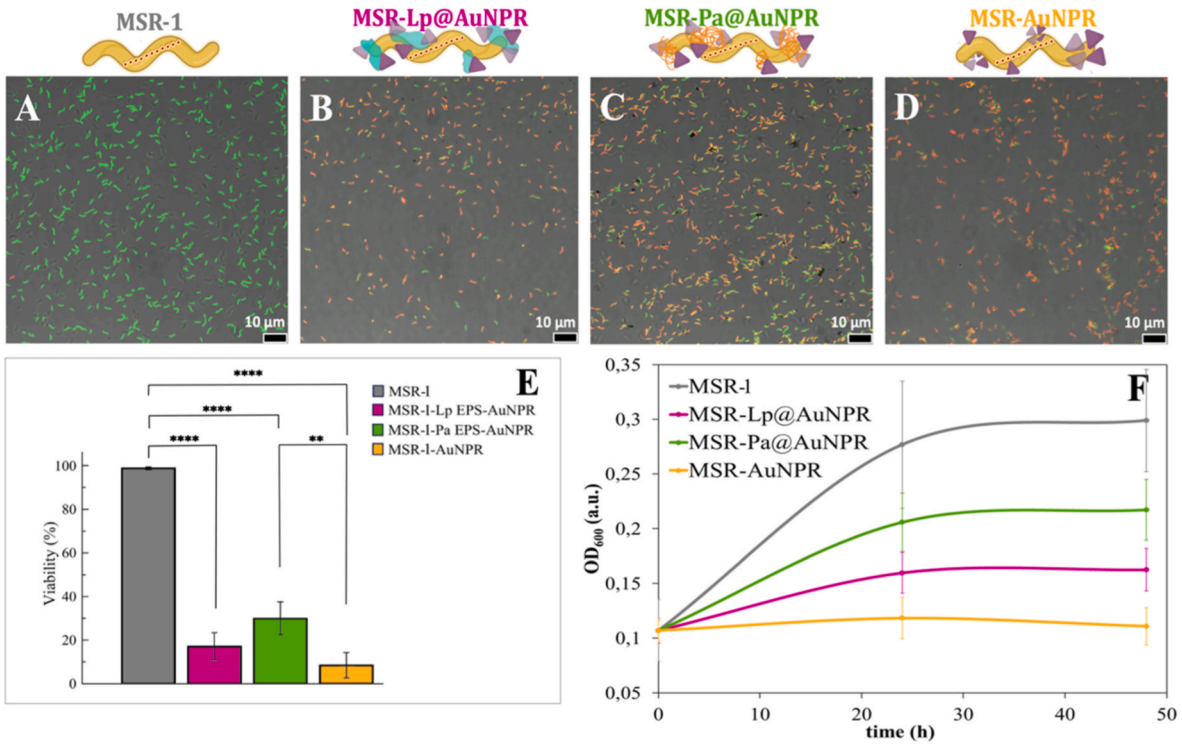

Fig. 7. Confocal laser scanning microscopy images of: (A) MSR-1, (B) MSR-Lp@AuNPR, (C) MSR-Pa@AuNPR and (D) MSR-AuNPR (Scale bars 10 µm). All images correspond to merged channels (green, live bacteria and red, dead bacteria). (E) % Viability of MSR-1, MSR-Lp@AuNPR, MSR-Pa@AuNPR and MSR-AuNPR obtained by counting live (green) and dead (red) bacteria from CLSM images. Asterisks represent significant differences (**$p < 0.01$; ***$p < 0.0001$). (F) Dynamic growth curves of MSR-1, MSR-Pa@AuNPR, MSR-Lp@AuNPR and MSR-AuNPR showing the effect of incorporation of isolated AuNPR (yellow solid line) or EPS-encapsulated AuNPR (pink solid line and green solid line).

that the samples releasing higher amounts of gold (MSR-AuNPR and MSR-Lp@AuNPR) are those that induce greater mortality in magnetotactic bacteria, which can be attributed to the cytotoxic nature both of Au^{3+} and AuNPs [43,44].

The live/dead assay provided information on the integrity of the bacterial wall but did not indicate whether MSR-1 were metabolically or physiologically active. To further assess the viability of MSR-1 after AuNPR attachment, measurements of bacterial growth were made by recording the optical density at a wavelength of 600 nm every 24 h from a control culture of MSR-1 as well as all systems including AuNPR. Bacterial growth curves of MSR-1, MSR-AuNPR, MSR-Lp@AuNPR and MSR-Pa@AuNPR are shown in Fig. 7F. The results were consistent with those previously obtained using CLSM. At the end time point (48 h), as usual MSR-1 reached the highest number of bacteria followed by MSR-Pa@AuNPR, MSR-Lp@AuNPR and MSR-AuNPR in that order. The initial number of bacteria in all the samples was $2.1x10^8$ bacteria/ml. After 48 h, amounts of 7.2, 5.1, 3.7 and $2.4x10^8$ bacteria/ml were recovered for MSR-1, MSR-Pa@AuNPR, MSR-Lp@AuNPR and MSR-AuNPR, respectively. The number of bacteria in MSR-AuNPR remained almost constant throughout the experiment, indicating a significant disruption of the metabolic machinery of MSR-1. This again demonstrates that EPS encapsulation of AuNPR provides protection against their cytotoxic effects.

These results demonstrated that the toxic effect of isolated AuNPRs on MSR-1 was significantly higher than that observed when AuNPRs were delivered within EPS. This protective role of the EPS coating appears to arise from several complementary mechanisms.

First, EPS acts as a stabilizing matrix for AuNPRs (Fig. 4). By stabilizing AuNPRs, EPS reduces their direct interaction with the bacterial membrane, thereby limiting physical disruption and DNA or membrane damage, which has been reported as major toxicity pathways of AuNPs in bacteria [44].

Secondly, the prevention of AuNPRs degradation is of significant importance, given the high toxicity of Au^{3+} to bacteria, including MSR-1. Remarkably, even low Au concentrations are able to inhibit bacterial growth.

Third, EPS possesses reducing capacity, limiting the toxic effect of Au^{3+} ions that may be released from the particles [27]. The reducing capacity of EPS decreases the presence of Au^{3+} ions, mitigating oxidative and ion-related stress.

Taken together, these results indicate that EPS works both as a chemical shield—by reducing free Au^{3+} ions—and as a physical barrier—by controlling nanoparticle stability and limiting direct membrane contact—therefore mitigating AuNPR-induced toxicity in MSR-1.

4. Conclusions

The functionalization of MSR-1 with AuNPR occurred through two distinct methodologies: i) a one-step procedure involving direct functionalization with AuNPR to yield MSR-AuNPR, and ii) a layer-by-layer approach, where AuNPR were pre-coated with EPS of L. plantarum or *P. aeruginosa*, and then incorporated to MSR-1, leading to MSR-Lp@AuNPR and MSR-Pa@AuNPR, respectively. It was demonstrated that the AuNPR produced an increase in temperature of approximately 8–10 °C when irradiated with NIR light (1064 nm). Interestingly, while the incorporation of AuNPR had a significant impact on the viability of MSR-1, the viability was improved when AuNPR were pre-coated with EPS. Furthermore, AuNPR-functionalized MSR-1 systems demonstrated low AuNPR-release profiles under biological conditions and exhibited satisfactory stability during prolonged cold storage. These findings expand the scope of functionalized magnetotactic bacteria for PTT, as the incorporation of AuNPR enhances the previously documented pathway of heating due to native magnetosomes.

The MSR-AuNPR and MSR-EPS@AuNPR biohybrid systems showed

strong translational potential as a new generation of hyperthermia agents by combining magnetosome-driven heating with AuNPR-mediated photothermal conversion, enabling adaptable activation modes tailored to tumor depth and accessibility. Its intrinsic targeting ability, stability, and low nanoparticle release make it a promising candidate for personalized cancer therapy, with opportunities to expand into theragnostic and controlled drug delivery. However, key challenges including the biosafety and clearance of MSR-1, the improvement of nanoparticle location and light penetration, and the development scalable, standardized production methods require further developments. Therefore, this work encourages further studies of these systems to overcome these hurdles, which will be essential for advancing this dual-mode platform towards clinical application.

CRediT authorship contribution statement

Laura Cerezo-Collado: Writing – review & editing, Methodology, Investigation. **Emilio Gómez:** Methodology, Investigation. **Yilian Fernández-Afonso:** Writing – review & editing, Methodology, Investigation. **Ana González:** Writing – review & editing, Methodology, Investigation. **Lucía Gutiérrez:** Writing – review & editing, Supervision, Methodology, Investigation. **Jesús M. de la Fuente:** Writing – review & editing, Methodology, Investigation. **Ana Abad:** Writing – review & editing, Methodology, Investigation. **Alicia G. Gubieda:** Writing – review & editing, Methodology, Investigation, Formal analysis. **Ma Luisa Fdez-Gubieda:** Writing – review & editing, Supervision, Investigation, Conceptualization. **Jose M. Dominguez-Vera:** Writing – review & editing, Supervision, Investigation, Funding acquisition, Conceptualization. **Víctor Garcés:** Writing – review & editing, Writing – original draft, Methodology, Investigation, Formal analysis, Conceptualization.

Declaration of competing interest

The authors declare that they have no known competing financial interests or personal relationships that could have appeared to influence the work reported in this paper.

Acknowledgements

This work was funded by the Ministerio de Universidades (MCIU), the Agencia Estatal de Investigación (AEI) and Fondo Europeo de Desarrollo Regional (FEDER) through the projects PID2019- 111461 GB-I00 to J.M.D-V. and PID2023-146448OB-21 to M.L.F-G., A.A. and A.G.G. Also, by the Basque Government through the project IT-1479-22. Project CNS2023-144321 funded by MICIU/AEI/10.13039/501100011033 and NextGenerationEU/PRTR, and Fondo Social del Gobierno de Aragón (grupo DGA E15-23R) are also acknowledged. V.G. acknowledges for the postdoctoral contract within the Margarita Salas 2021 program (Universidad de Granada-Ministerio de Universidades-Next Generation EU). Y.F-A. thanks Santander-Universidad Zaragoza Fellowship program for her PhD position. Authors would like to acknowledge the use of Servicio General de Apoyo a la Investigación-SAI, Universidad de Zaragoza. The authors also wish to acknowledge the Scientific Instrumentation Centre (CIC) of the University of Granada for access to its facilities.

Appendix A. Supplementary data

Supplementary data to this article can be found online at https://doi.org/10.1016/j.mtchem.2025.103178.

Data availability

Data for this article are available at Zenodo, the institutional repository from European Commission, at https://doi.org/10.5281/zenodo.13151054.

References

[1] F.K. Storm, W.H. Harrison, R.S. Elliott, D.L. Morton, Normal tissue and solid tumor effects of hyperthermia in animal models and clinical trials, Cancer Res. 39 (1979) 2245–2251.
[2] Y. Wang, Y. Xu, J. Song, X. Liu, S. Liu, N. Yang, L. Wang, Y. Liu, Y. Zhao, W. Zhou, Y. Zhang, Tumor Cell-Targeting, Tumor Microenvironment–Responsive, Nanoplatforms for the multimodal imaging-guided photodynamic/photothermal/chemodynamic treatment of cervical cancer, int, J. Nanomedicine 19 (2024) 5837–5858, https://doi.org/10.2147/IJN.S466042.
[3] X. Han, C. Zhao, S. Wang, Z.Y. Pan, Z. Jiang, X. Tang, Multifunctional TiO2/C nanosheets derived from 3D metal–organic frameworks for mild-temperature-photothermal-sonodynamic-chemodynamic therapy under photoacoustic image guidance, J. Colloid Interface Sci. 621 (2022) 360–373, https://doi.org/10.1016/j.jcis.2022.04.077.
[4] A. Espinosa, J. Kolosnjaj-Tabi, A. Abou-Hassan, A. Plan Sangnier, A. Curcio, A.K. A. Silva, R. Di Corato, S. Neveu, T. Pellegrino, L.M. Liz-Marzán, C. Wilhelm, Magnetic (hyper)Thermia or photothermia? Progressive comparison of iron oxide and gold nanoparticles heating in water, in cells, and in vivo, Adv. Funct. Mater. 28 (2018) 1–16, https://doi.org/10.1002/adfm.201803660.
[5] H. Kim, Y.R. Lee, H. Jeong, J. Lee, X. Wu, H. Li, J. Yoon, Photodynamic and photothermal therapies for bacterial infection treatment, Smart Mol. 1 (2023), https://doi.org/10.1002/smo.20220010.
[6] J.B. Vines, J.H. Yoon, N.E. Ryu, D.J. Lim, H. Park, Gold nanoparticles for photothermal cancer therapy, Front. Chem. 7 (2019) 1–16, https://doi.org/10.3389/fchem.2019.00167.
[7] B. Pelaz, V. Grazu, A. Ibarra, C. Magen, P. del Pino, J.M. de la Fuente, Tailoring the synthesis and heating ability of gold nanoprisms for bioapplications, Langmuir 28 (2012) 8965–8970, https://doi.org/10.1021/la204712u.
[8] C. Yu, F. Wo, Y. Shao, X. Dai, M. Chu, Bovine serum albumin nanospheres synchronously encapsulating gold selenium/gol nanoparticles and photosensitizer for high-efficiency cancer phototherapy, Appl. Biochem. Biotechnol. 169 (2013) 1566–1578, https://doi.org/10.1007/s12010-012-0078-x.
[9] X. Huang, P.K. Jain, I.H. El-Sayed, M.A. El-Sayed, Plasmonic photothermal therapy (PPTT) using gold nanoparticles, Lasers Med. Sci. 23 (2008) 217–228, https://doi.org/10.1007/s10103-007-0470-x.
[10] M.L. Fdez-Gubieda, J. Alonso, A. García-Prieto, A. García-Arribas, L. Fernández Barquín, A. Muela, Magnetotactic bacteria for cancer therapy, J. Appl. Phys. 128 (2020), https://doi.org/10.1063/5.0018036.
[11] R. Blakemore, Magnetotactic bacteria, Science 190 (1975) 377–379, https://doi.org/10.1126/science.170679.
[12] T. Sakaguchi, J.G. Burgess, T. Matsunaga, Magnetite formation by a sulphate-reducing bacterium, Nature 365 (1993) 47–49, https://doi.org/10.1038/365047a0.
[13] D. Schüler, Genetics and cell biology of magnetosome formation in magnetotactic bacteria, FEMS Microbiol. Rev. 32 (2008) 654–672, https://doi.org/10.1111/j.1574-6976.2008.00116.x.
[14] R. Uebe, D. Schüler, Magnetosome biogenesis in magnetotactic bacteria, Nat. Rev. Microbiol. 14 (2016) 621–637, https://doi.org/10.1038/nrmicro.2016.99.
[15] T. Gwisai, N. Mirkhani, M.G. Christiansen, T.T. Nguyen, V. Ling, S. Schuerle, Magnetic torque-driven living microrobots for enhanced tumor infiltration authors, Sci. Robot. 7 (2022) eabo0665, https://doi.org/10.1126/scirobotics.abo0665.
[16] O. Felfoul, M. Mohammadi, S. Taherkhani, D. De Lanauze, Y. Zhong Xu, D. Loghin, S. Essa, S. Jancik, D. Houle, M. Lafleur, L. Gaboury, M. Tabrizian, N. Kaou, M. Atkin, T. Vuong, G. Batist, N. Beauchemin, D. Radzioch, S. Martel, Magneto-aerotactic bacteria deliver drug-containing nanoliposomes to tumour hypoxic regions, Nat. Nanotechnol. 11 (2016) 941–947, https://doi.org/10.1038/nnano.2016.137.
[17] E. Alphandéry, S. Faure, O. Seksek, F. Guyot, I. Chebbi, Chains of magnetosomes extracted from AMB-1 magnetotactic bacteria for application in alternative magnetic field cancer therapy, ACS Nano 5 (2011) 6279–6296, https://doi.org/10.1021/nn201290k.
[18] D. Gandia, L. Gandarias, I. Rodrigo, J. Robles-García, R. Das, E. Garaio, J.Á. garcía, M.H. phan, H. Srikanth, I. Orue, J. Alonso, A. muela, M.L. fdez-gubieda, unlocking the potential of magnetotactic bacteria as magnetic hyperthermia agents, Small 15 (2019), https://doi.org/10.1002/smll.201902626.
[19] D. Villanueva, A.G. Gubieda, A. Abad, I. Orue, A. Garc, D. De Cos, J. Alonso, M. L. Fdez-gubieda, Heating efficiency of different magnetotactic bacterial species: influence of magnetosome morphology and chain arrangement. https://doi.org/10.1021/acsami.4c13152, 2024.
[20] G. Huang, G. Zhu, R. Lin, W. Chen, R. Chen, Y. Sun, L. Chen, D. Hong, L. Chen, Magnetotactic bacteria AMB-1 with active deep tumor penetrability for NIR-II photothermal tumor therapy, ACS Omega 9 (2024) 23060–23068, https://doi.org/10.1021/acsomega.4c02914.
[21] A. Espinosa, J. Reguera, A. Curcio, Á. Muñoz-Noval, C. Kuttner, A. Van de Walle, L. M. Liz-Marzán, C. Wilhelm, Janus Magnetic-Plasmonic Nanoparticles for Magnetically Guided and Thermally Activated Cancer Therapy, Small 16 (2020) 1–14, https://doi.org/10.1002/smll.201904960.
[22] S.K. Alsaiari, A.H. Ezzedine, A.M. Abdallah, R. Sougrat, N.M. Khashab, Magnetotactic bacterial cages as safe and smart gene delivery vehicles, OpenNano 1 (2016) 36–45, https://doi.org/10.1016/j.onano.2016.07.001.
[23] P. Ye, F. Li, J. Zou, Y. Luo, S. Wang, G. Lu, F. Zhang, C. Chen, J. Long, R. Jia, M. Shi, Y. Wang, X. Cheng, G. Ma, W. Wei, In Situ generation of gold nanoparticles on bacteria-derived magnetosomes for imaging-guided starving/chemodynamic/photothermal synergistic therapy against cancer, Adv. Funct. Mater. 32 (2022), https://doi.org/10.1002/adfm.202110063.

[24] C. Chen, L. Chen, Y. Yi, C. Chen, L.F. Wu, T. Song, Killing of Staphylococcus aureus via magnetic hyperthermia mediated by magnetotactic bacteria, Appl. Environ. Microbiol. 82 (2016) 2219–2226, https://doi.org/10.1128/AEM.04103-15.
[25] V. Garcés, A. González, N. Gálvez, J.M. Delgado-López, J.J. Calvino, S. Trasobares, Y. Fernández-Afonso, L. Gutiérrez, J.M. Dominguez-Vera, Magneto-optical hyperthermia agents based on probiotic bacteria loaded with magnetic and gold nanoparticles, Nanoscale 14 (2022) 5716–5724, https://doi.org/10.1039/d1nr08513a.
[26] M.L. Fdez-Gubieda, A. Muela, J. Alonso, A. García-Prieto, L. Olivi, R. Fernández-Pacheco, J.M. Barandiarán, Magnetite biomineralization in magnetospirillum gryphiswaldense: Time-Resolved magnetic and structural studies, ACS Nano 7 (2013) 3297–3305, https://doi.org/10.1021/nn3059983.
[27] A. González, V. Garcés, L. Sabio, F. Velando, M. López-Haro, N. Gálvez, J. J. Calvino, J.M. Dominguez-Vera, Optical and tomography studies of water-soluble gold nanoparticles on bacterial exopolysaccharides, J. Appl. Phys. 126 (2019), https://doi.org/10.1063/1.5090879.
[28] P.M. Bales, E.M. Renke, S.L. May, Y. Shen, D.C. Nelson, Purification and characterization of biofilm-associated EPS exopolysaccharides from ESKAPE organisms and other pathogens, PLoS One 8 (2013), https://doi.org/10.1371/journal.pone.0067950.
[29] X. Guo, W. Li, H. Wang, Y.Y. Fan, H. Wang, X. Gao, B. Niu, X. Gong, Preparation, characterization, release and antioxidant activity of curcumin-loaded amorphous calcium phosphate nanoparticles, J. Non-Cryst. Solids 500 (2018) 317–325, https://doi.org/10.1016/j.jnoncrysol.2018.08.015.
[30] S.L. Jacques, Erratum: optical properties of biological tissues: a review (Physics in Medicine and biology (2013) 58), Phys. Med. Biol. 58 (2013) 5007–5008, https://doi.org/10.1088/0031-9155/58/14/5007.
[31] Y. Liu, J. Kangas, Y. Wang, K. Khosla, J. Pasek-Allen, A. Saunders, S. Oldenburg, J. Bischof, Photothermal conversion of gold nanoparticles for uniform pulsed laser warming of vitrified biomaterials, Nanoscale 12 (2020) 12346–12356, https://doi.org/10.1039/d0nr01614d.
[32] R. Zhang, H. Lin, Z. Wang, S. Cheng, C. Li, Y. Wang, Research progress on antimicrobial biomaterials, macromol, Biosci (2025), https://doi.org/10.1002/mabi.202500239.
[33] J. Wang, H. Ji, S. Wang, H. Liu, W. Zhang, D. Zhang, Y. Wang, Probiotic Lactobacillus plantarum promotes intestinal barrier function by strengthening the epithelium and modulating gut microbiota, Front. Microbiol. 9 (2018) 1–14, https://doi.org/10.3389/fmicb.2018.01953.
[34] K. Myszka, K. Czaczyk, Characterization of adhesive exopolysaccharide (EPS) produced by Pseudomonas aeruginosa under starvation conditions, Curr. Microbiol. 58 (2009) 541–546, https://doi.org/10.1007/s00284-009-9365-3.
[35] N.S. Kiran, C. Yashaswini, S. Singh, B.G. Prajapati, Revisiting microbial exopolysaccharides: a biocompatible and sustainable polymeric material for multifaceted biomedical applications, 3 Biotech 14 (2024) 1–24, https://doi.org/10.1007/s13205-024-03946-3.
[36] Z. Liu, Z. Zhang, L. Qiu, F. Zhang, X. Xu, H. Wei, X. Tao, Characterization and bioactivities of the exopolysaccharide from a probiotic strain of Lactobacillus plantarum WLPL04, J. Dairy Sci. 100 (2017) 6895–6905, https://doi.org/10.3168/jds.2016-11944.
[37] S. Rathinasamy, S. Annamalai, Characterization of extracellular polymeric substances (EPS) produced by Pseudomonas aeruginosa, Int. J. Mech. Eng. 7 (2022) 974–5823.
[38] Y. Fernandez-Afonso, L. Asın, J. Pardo, R.M. Fratila, S. Veintemillas, M.P.Morales and l.Gutierrez, key factors influencing magnetic nanoparticlebased photothermal therapy: physicochemical properties, irradiation power, and particle concentration in vitro, Nanoscale Adv. (2024), https://doi.org/10.1039/d4na00384e.
[39] X. He, S. Zhang, Y. Tian, W. Cheng, H. Jing, Research progress of nanomedicine-based mild photothermal therapy in tumor. https://doi.org/10.2147/IJN.S405020, 2023.
[40] R. López-Méndez, J. Reguera, A. Fromain, E.S.A. Serea, E. Céspedes, F.J. Teran, F. Zheng, A. Parente, M.Á. garcía, E. Fonda, J. Camarero, C. Wilhelm, Á. muñoz-noval, A. Espinosa, X-Ray nanothermometry of nanoparticles in tumor-mimicking tissues under photothermia, Adv. Healthc. Mater 12 (2023) 1–10, https://doi.org/10.1002/adhm.202301863.
[41] S. Nomura, Y. Morimoto, H. Tsujimoto, M. Arake, M. Harada, D. Saitoh, I. Hara, E. Ozeki, A. Satoh, E. Takayama, K. Hase, Y. Kishi, H. Ueno, Highly reliable, targeted photothermal cancer therapy combined with thermal dosimetry using a near-infrared absorbent, Sci. Rep. 10 (2020) 1–7, https://doi.org/10.1038/s41598-020-66646-x.
[42] C. Mesas, V. Garcés, R. Martínez, R. Ortiz, K. Doello, J.M. Dominguez-Vera, F. Bermúdez, J.M. Porres, M. López-Jurado, C. Melguizo, J.M. Delgado-López, J. Prados, Colon cancer therapy with calcium phosphate nanoparticles loading bioactive compounds from euphorbia lathyris: in vitro and in vivo assay, Biomed. Pharmacother. 155 (2022), https://doi.org/10.1016/j.biopha.2022.113723.
[43] V. Bansal, A. Bharde, R. Ramanathan, S.K. Bhargava, Inorganic materials using “unusual” microorganisms, adv. Colloid Interface Sci, 179–182 (2012) 150–168, https://doi.org/10.1016/j.cis.2012.06.013.
[44] P. Ray, T. Lodha, A. Biswas, T.K. Sau, C.V. Ramana, Particle specific physical and chemical effects on antibacterial activities: a comparative study involving gold nanostars, nanorods and nanospheres, colloids surfaces A physicochem, Eng. Asp. 634 (2022) 127915, https://doi.org/10.1016/j.colsurfa.2021.127915.